Automaticity in acute ischemia: Bifurcation analysis of a human ventricular model

Sylvain Bouchard, Vincent Jacquemet, and Alain Vinet
Institut de Génie Biomédical, Department of Physiology, Faculty of Medicine, Université de Montréal and Centre de Recherche, Hôpital du Sacré-Coeur, 5400 Gouin W. (Montréal), Canada, H4J 1C5
(Received 7 September 2010; revised manuscript received 8 November 2010; published 18 January 2011)

Acute ischemia (restriction in blood supply to part of the heart as a result of myocardial infarction) induces major changes in the electrophysiological properties of the ventricular tissue. Extracellular potassium concentration ($[K_o^+]$) increases in the ischemic zone, leading to an elevation of the resting membrane potential that creates an "injury current" (I_S) between the infarcted and the healthy zone. In addition, the lack of oxygen impairs the metabolic activity of the myocytes and decreases ATP production, thereby affecting ATP-sensitive potassium channels (I_{Katp}). Frequent complications of myocardial infarction are tachycardia, fibrillation, and sudden cardiac death, but the mechanisms underlying their initiation are still debated. One hypothesis is that these arrhythmias may be triggered by abnormal automaticity. We investigated the effect of ischemia on myocyte automaticity by performing a comprehensive bifurcation analysis (fixed points, cycles, and their stability) of a human ventricular myocyte model [K. H. W. J. ten Tusscher and A. V. Panfilov, Am. J. Physiol. Heart Circ. Physiol. **291**, H1088 (2006)] as a function of three ischemia-relevant parameters $[K_o^+]$, I_S, and I_{Katp}. In this single-cell model, we found that automatic activity was possible only in the presence of an injury current. Changes in $[K_o^+]$ and I_{Katp} significantly altered the bifurcation structure of I_S, including the occurrence of early-after depolarization. The results provide a sound basis for studying higher-dimensional tissue structures representing an ischemic heart.

DOI: 10.1103/PhysRevE.83.011911 PACS number(s): 87.19.Hh

I. INTRODUCTION

Even though death rates from cardiovascular disease have declined in recent years, it is estimated that 935 000 Americans will suffer from myocardial infarction (MI) in 2010 [1]. As a result of the blockade of a coronary artery, MI is characterized by a lack of blood flow creating an ischemic zone where myocytes have impaired excitability. Acute ischemia, corresponding to the first phase (∼15 minutes) following the perfusion default, involves multiple changes in the electrical or ionic characteristics of the cells (see Ref. [2] for review), which can lead to ventricular tachycardia, arrhythmia, or fibrillation. It remains the most common cause of sudden cardiac death.

ST segment elevation, a hallmark of MI, has been used as a diagnostic tool for decades. One theory explaining ST elevation is that the increase in membrane potential (V), resulting notably from the accumulation of potassium ions in the extracellular space, leads to a decrease of the diastolic baseline of electrocardiogram (ECG) [3] and would be observed as ST segment elevation in an AC-coupled ECG. Another hypothesis is that it is produced by the flow of injury current following from the difference in membrane potential between healthy and ischemic tissue [4]. It was also found, in a knockout animal model, that the absence of an ATP-sensitive potassium channel (I_{Katp}) leads to a marked decrease in ST elevation [5]. Mathematical modeling of ischemia [6] has also suggested I_{Katp} to be the main ion channel responsible for the shortening of action potential duration observed experimentally.

The injury current is pro-arrhythmic and could be responsible for automatic or ectopic activity in the border zone of the infarct, where it is maximal. Ectopic activation, believed to be a key factor leading to arrhythmia [7], may happen if a group of myocytes switches from normal excitable cells to oscillators. This could activate adjacent cells and start the arrhythmia.

As an initial step toward investigating ectopic activity in tissue embedding an ischemic zone, we studied the effect of three ischemia-related parameters on the quiescent and oscillatory states of the ten Tusscher, Noble, Noble, and Panfilov model of isolated human ventricular cardiac myocytes (TNNP) [8,9]. First, the effect of hyperkalemia (i.e., increased extracellular potassium, $[K_o^+]$) was studied. From a normal value of 5.4mM, it may increase to 15mM within the first minutes of the ischemic injury [10,11]. The difference in extracellular potassium concentration between the ischemic and healthy zone also imposes a gradient of diastolic potential [12], resulting in an injury current. It was modeled by adding an inward K^+ bias current (I_S). Finally, an ATP-inactivated potassium channel was added to the model, whose maximum conductance was varied to represent the effect of anoxia [13–15]. In several modeling works, the ischemic zone has been represented by a spatial profile of $[K_o^+]$ and/or G_{Katp} [12,16,17]. Herein, we rather provide a comprehensive description of the effect of these parameters on the autonomous solutions of a single cell.

II. METHODS

A. Ventricular cell model

The epicardial variant of the 2006 TNNP model [9] was used because the epicardium is the region most directly affected by ischemia [2,18,19]. It is a second-generation cardiac ionic model that includes the dynamics of the cytoplasmic concentrations $[Na^+]_i$, $[K^+]_i$, and $[Ca^{++}]_i$ and the calcium concentration in intracellular compartments representing the sarcoplasmic reticulum (SR), $[Ca^{++}]_{\mathrm{sr}}$, and the dyadic compartment (subspace/SS), $[Ca^{++}]_{\mathrm{ss}}$. The evolution

of the concentrations is governed by ionic currents through the cell membrane and fluxes between the compartments, namely:

$$\begin{aligned}
\frac{d[\mathrm{Ca}^{++}]_i}{dt} &= \frac{C_t}{2V_cF}(2I_{\mathrm{NaCa}} - I_{b\mathrm{Ca}} - I_{p\mathrm{Ca}}) \\
&\quad + \frac{V_{\mathrm{sr}}}{V_c}(I_{\mathrm{leak}} - I_{\mathrm{up}}) + I_{\mathrm{xfer}}, \\
\frac{d[\mathrm{Ca}^{++}]_{\mathrm{sr}}}{dt} &= I_{\mathrm{up}} - I_{\mathrm{rel}} - I_{\mathrm{leak}}, \\
\frac{d[\mathrm{Ca}^{++}]_{\mathrm{ss}}}{dt} &= \frac{V_{\mathrm{sr}}}{V_{\mathrm{ss}}}I_{\mathrm{rel}} - \frac{C_t}{2V_{\mathrm{ss}}F}I_{\mathrm{CaL}} - \frac{V_c}{V_{\mathrm{ss}}}I_{\mathrm{xfer}}, \\
\frac{d[\mathrm{Na}^{+}]_i}{dt} &= -\frac{C_t}{V_cF}(I_{\mathrm{Na}} + I_{b\mathrm{Na}} + 3I_{\mathrm{NaK}} + 3I_{\mathrm{NaCa}}), \\
\frac{d[\mathrm{K}^{+}]_i}{dt} &= -\frac{C_t}{V_cF}(I_{\mathrm{K1}} + I_{to} + I_{\mathrm{K}r} + I_{\mathrm{K}s} - 2I_{\mathrm{NaK}} \\
&\quad + I_{p\mathrm{K}} + I_S + I_{\mathrm{Katp}}),
\end{aligned} \tag{1}$$

where C_t is the membrane capacitance, F is Faraday's constant, and V_C, V_{sr}, and V_{ss} are the volume of the cytoplasm, sarcoplasmic reticulum, and subspace, respectively.

The model incorporates a representation of calcium-induced calcium release (CICR) [20,21]. The release depends on the free calcium concentration in both the SR ($[\mathrm{Ca}^{++}]_{\mathrm{sr}}$) and the dyadic compartment ($[\mathrm{Ca}^{++}]_{\mathrm{ss}}$). The calcium entering the SS from both the SR (I_{rel}) and the membrane calcium channels (I_{CaL}) flows to the cytoplasm (I_{xfer}), from which it can be taken up again by the SR (I_{up}). There is also a leaking current (I_{leak}) between the cytoplasm and the SR, proportional to the difference between $[\mathrm{Ca}^{++}]_i$ and $[\mathrm{Ca}^{++}]_{\mathrm{sr}}$.

The membrane currents are voltage dependent. Their channel conductance is modulated by gating variables y satisfying equations of the form [22]

$$\frac{dy}{dt} = \frac{y_\infty - y}{\tau_y}, \tag{2}$$

where y_∞ and τ_y are voltage-dependent (or concentration-dependent for some calcium currents) functions. In the range of membrane potentials (V) investigated in the present study, cytoplasmic concentrations are mainly regulated by I_{K1}, $I_{\mathrm{K}r}$, $I_{\mathrm{K}s}$, and I_{CaL}, as well as the sodium-calcium and sodium-potassium exchangers (I_{NaCa}, I_{NaK}).

Since it is known to shorten significantly the action potential during ischemia, a potassium ATP-inactivated current (I_{Katp}) was added to the original TNNP model. Because I_{Katp} density and conductivity in human myocytes are not well known, we used a simplifed formulation of the model of Michailova *et al.* [15], which they adjusted to reproduce action potential shortening in pig myocytes:

$$I_{\mathrm{Katp}} = G_{\mathrm{Katp}}G_{\mathrm{maxKatp}}([K_o^+]/[K^+_{\mathrm{onormal}}])^{0.24}(V - E_k), \tag{3}$$

where $[K^+_{\mathrm{onormal}}] = 5.4\mathrm{m}M$ and $G_{\mathrm{maxKatp}} = 0.05\ \mathrm{mS}/\mu F$, which is the maximum conductance of the current in their model. The extracellular potassium concentration $[\mathrm{K}_o^+]$ and the normalized ATP-dependent conductance G_{Katp} are fixed parameters.

During ischemia, there is an accumulation of $[\mathrm{K}_o^+]$ in the ischemic zone, leading to an increase of the membrane potential. This creates a flow of current between the injured and healthy zone. In this study, this effect was modeled as a time- and voltage-independent bias potassium current $I_S(\mathrm{K}^+)$.

The evolution of the membrane potential V is determined by the membrane currents:

$$\begin{aligned}
C_t\frac{dV}{dt} &= I_{\mathrm{Na}} + I_{\mathrm{K1}} + I_{to} + I_{\mathrm{K}r} + I_{\mathrm{K}s} + I_{\mathrm{CaL}} + I_{\mathrm{NaCa}} \\
&\quad + I_{\mathrm{NaK}} + I_{p\mathrm{Ca}} + I_{p\mathrm{K}} + I_{b\mathrm{Ca}} + I_{b\mathrm{Na}} + I_S + I_{\mathrm{Katp}}.
\end{aligned} \tag{4}$$

With the addition of this equation, the Jacobian matrix of the full system becomes singular [23]. Indeed, if the membrane potential is set to

$$\begin{aligned}
V &= \frac{V_c}{C_tF}([\mathrm{Na}^+]_i + 2[\mathrm{Ca}^{++}]_i + [K^+]_i) + \frac{V_{\mathrm{sr}}}{C_tF}2[\mathrm{Ca}^{++}]_{\mathrm{sr}} \\
&\quad + \frac{V_{\mathrm{ss}}}{C_tF}2[\mathrm{Ca}^{++}]_{\mathrm{ss}} + V_0,
\end{aligned} \tag{5}$$

Eq. (4) can be derived from the concentration equations (1). The constant V_0 can be computed using the initial condition from Ref. [9]. Note that this algebraic formulation for the membrane potential requires stimulation and bias currents to be attributed to specific ionic species. The complete set of equations and parameters of the model are available as an online supplement [24].

B. Bifurcation analysis

The TNNP model consists of an 18-dimensional system of autonomous ordinary differential equations [5 concentrations and 13 gating variables, the membrane potential being computed using the algebraic relation (5)]. This system can be formally written as

$$\frac{d\mathbf{X}}{dt} = \frac{d}{dt}\begin{bmatrix} x_1 \\ \vdots \\ x_{18} \end{bmatrix} = \mathbf{F}(\mathbf{X}) = \begin{bmatrix} f_1(\mathbf{X}) \\ \vdots \\ f_{18}(\mathbf{X}) \end{bmatrix}. \tag{6}$$

The fixed points $\mathbf{X_f}$ of the system, fulfilling the relation $\mathbf{F}(\mathbf{X_f}) = 0$, are stable or unstable depending on whether the trajectory returns or departs from $\mathbf{X_f}$ after a perturbation. Following any infinitesimal perturbation $\mathbf{Y}$ around $\mathbf{X_f}$, the dynamics can be described by the linear system

$$\frac{d\mathbf{Y}}{dt} = \mathbf{J}\,\mathbf{Y}, \tag{7}$$

where $\mathbf{J}$ is the Jacobian matrix containing the partial derivatives of the functions evaluated at $\mathbf{X_f}$, i.e, $J_{i,j} = (\partial f_i/\partial x_j)|_{\mathbf{X_f}}$. The local stability is controlled by the real part of the eigenvalues of $\mathbf{J}$. $\mathbf{X_f}$ is unstable if there is at least one eigenvalue with positive real part. Removing from $\mathbf{J}$ the line and the column associated with a variable (i.e., $J_{i,j}$ and $J_{j,i}$ for all j) amounts to assuming that it adjusts instantaneously to fulfill the relation $f_i(\mathbf{X}) = 0$, such that its own dynamics is no longer involved in the stability of the fixed point.

Periodic solutions of the system can also be stable or unstable. The local stability of a periodic orbit can be assessed by tracking the dynamics after a perturbation $\mathbf{Y}$ relative to a reference point $\mathbf{X_r}$ on the cycle. The positions of the successive returns $\mathbf{Y}_i$ relative to $\mathbf{X_r}$ in a plane normal to the orbit define

an iterative 17-dimensional system:

$$\mathbf{Y}_{i+1} = \mathbf{A}\,\mathbf{Y}_i. \tag{8}$$

The amplitude of $\mathbf{Y}_i$ wanes if the modulus of the eigenvalues of $\mathbf{A}$, referred to as Floquet's multipliers, is less than one. (See Refs. [25–27] for introductory or advanced textbooks on stability theory.)

The aim of this paper is to study the evolution of the fixed points and cycles of the system as a function of three parameters relevant to ischemic conditions: the potassium injury current $I_S(K^+)$, the extracellular potassium concentration $[K_o^+]$, and the conductance of the potassium ATP-inactivated current G_{Katp}. Bifurcations occur at parameter values where either the number or the stability of the solutions changes.

The set of fixed points as a function of the parameters P can be obtained by solving the equation $F[\mathbf{X_f}(P)] = 0$. Starting from an initial condition $\mathbf{X_f}(P_0)$ (which in our case was a stable fixed point provided by simulation of the ODE system using the stiff MATLAB solver ode15s [28,29]), it becomes a continuation problem for which different numerical methods and freeware packages are available (see Ref. [30] for review). We have used the continuation software AUTO-07P [31] to prolong both the stable fixed points and cycles obtained by numerical simulations and diagnose their stability.

The pseudo-arc continuation method used by AUTO required the ODE system to be continuous. One inactivation gate variable (h) of sodium current (I_{Na}) has a discontinuity of the form:

$$h_\infty(V), \tau_h(V) = \begin{cases} f_1(V) & \text{if} \quad V \leqslant -40\ \text{mV} \\ f_2(V) & \text{if} \quad V > -40\ \text{mV}. \end{cases} \tag{9}$$

The functions h_∞ and τ_h were made continuous by connecting them by a sigmoid function centered at -40 mV:

$$f(V) = [1 - \Sigma(V)]\, f_2(V) + \Sigma(V)\, f_1(V), \tag{10}$$

$$\Sigma(V) = \frac{1}{(1 + e^{(V+40)})}. \tag{11}$$

The resulting continuous system displayed the same response as the original formulation upon current pulse stimulations.

C. Reduced models

Simplified versions of the TNNP model were also used to elucidate the processes responsible for the changes in stability of the fixed points and cycles:

(i) Model MnoSR: suppressing the SR dynamics by removing I_{leak}, I_{up}, I_{rel}, and $[Ca^{++}]_{sr}$. Sixteen variables: 12 gating variables, 4 ionic concentrations (1), and algebraic V (5).

(ii) Model MonlyCA: to study the dynamics of the intracellular calcium by suppressing all membrane currents. Four variables: $[Ca^{++}]_{sr}$, $[Ca^{++}]_{ss}$, $[Ca^{++}]_i$ (1), and one gating variable associated with the CICR. Everything else fixed at steady-state values of the complete TNNP model obtained for different sets of parameters.

(iii) Model MonlyV1: All concentrations frozen at their resting values for $I_S = 0$; I_{leak}, I_{up}, and I_{rel} removed, and V reinstated as a variable. Twelve variables: 11 gating variables and a differential equation for V (4).

(iv) Model MonlyV2: same as MonlyV1, but suppressing the voltage dependence of the potassium and calcium pumps.

III. RESULTS

A. Effect of I_S

1. Fixed points

The z-shaped diagram displaying the membrane potential (V) of the fixed points as a function of $I_S(K^+)$ [Fig. 1(a)] has three branches. This was also observed in simpler first-generation ventricular myocyte models subjected to a constant bias current [32,33]. Since the fixed points of TNNP model correspond to a Donnan equilibrium [34], the total flux of each ionic species must be zero, and I_S must be compensated by the outflow of $[K^+]$. I_{K1}, I_{Kr}, and I_{Ks} [Fig. 1(b)] are the main $[K^+]$ ionic currents involved in setting the equilibrium. I_{K1} and I_{Kr} have a bell-shaped steady-state current peaking around -50 and -20 mV, respectively, while I_{Ks} is an exponentially increasing current that dominates from ~ -30 mV. As a result, I_{K1} is the main supplier on the lower branch while I_{Ks} dominates on the far part of the upper branch. The middle and upper branches, in the interval where they coexist, are defined by two different mixtures of the three currents. The total outward K^+ flow provided by these currents is everywhere greater than I_S, and the resulting loss of K^+ is offset by the NaK exchanger. The latter also produces an outflow of Na^+ from the cell. Na^+ removal by I_{NaK} is chiefly balanced by the NaCa exchanger [Fig. 1(c)]. Since the NaCa exchanger removes one Ca^{++} for every three Na^+ that enters the cell, it produces a leak of Ca that is mostly balanced by the Ca^{++} injected in the dyadic space by I_{CaL} [Fig. 1(d)].

The membrane potential V of the resting points is set by the weighted sum of intracellular ionic concentrations [Fig. 1(e)]. Although the variation of the cytoplasmic $[Ca^{++}]$ appears minimal compared with the changes of $[Na_i^+]$ and $[K_i^+]$, it plays an important role in setting the equilibrium because of the high sensitivity of I_{NaCa} to $[Ca_i^{++}]$. It can be seen that the change of $[Na_i^+]$ and $[K_i^+]$ follows the curve of I_{CaL}. The inflow of $[Na^+]$ associated with the balance of

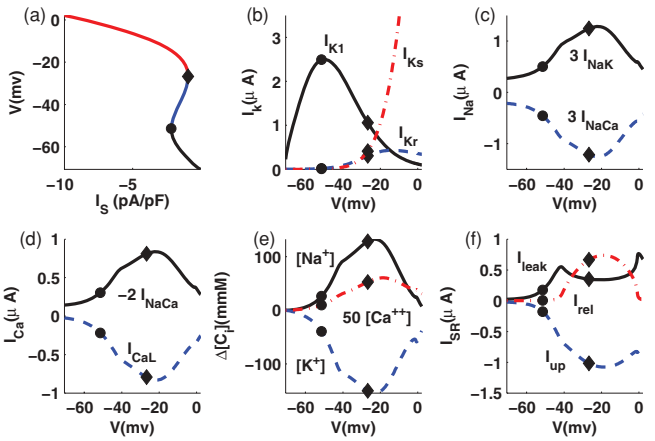

FIG. 1. (Color online) Fixed points of the TNNP model as a function of $I_S(K^+)$ ($K_o = 10$mM, $G_{Katp} = 0$). (a) V as a function of $I_S(K^+)$. The dot and the diamond, which are reproduced in each panel, locate the limits of the middle branch. As a function of V of the fixed points, (b) I_{K1}, I_{Kr}, and I_{Ks}; (c) $3I_{NaK}$ and $3I_{NaCa}$; (d) $-2I_{NaCa}$ and I_{CaL}; (e) $[Na_i^+]$, $[K_i^+]$, and $50[Ca_i^{++}]$, the last multiplied by 50 such that its variation could be seen; (f) the SR currents I_{leak}, I_{up}, and I_{rel}.

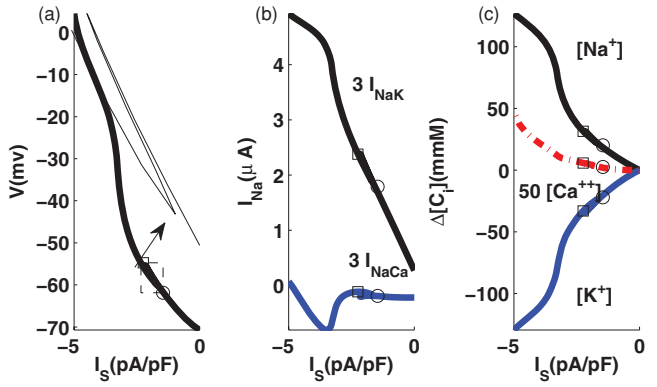

FIG. 2. (Color online) Fixed points of the TNNP model as a function of $I_S(\mathrm{Na}^+)$ ($\mathrm{K}_o = 10\mathrm{m}M$, $G_{\mathrm{Katp}} = 0$). (a) V (the thin line shows a zoom of the marked area), (b) $3I_{\mathrm{NaK}}$ and $3I_{\mathrm{NaCa}}$, (c) $[\mathrm{Na}_i^+]$, $[\mathrm{K}_i^+]$, and $50[\mathrm{Ca}_i^{++}]$.

I_{CaL} by I_{NaCa} requires an increase in I_{NaK}. I_{NaK} is a function only of V and $[\mathrm{Na}_i^+]$, being much more sensitive to the latter. Hence, $[\mathrm{Na}_i^+]$ increases and induces an outward flow of K^+, which reduces its concentration. The dynamics of the Ca^{++} also involve the SR and SS, the dyadic space. Figure 1(f) shows the evolution of the currents flowing in and out of the SR, which are involved in the stability of the fixed points, as it will be seen in the next section.

In a model of paced atrial cell, assigning the stimulation current to a specific ion has been shown to alter the transient and stable response of the system [23]. It also deeply modifies the location of the fixed points of the TNNP model, as shown in Fig. 2, for which I_S was allocated to Na^+. Na^+ is essentially removed by the NaK exchanger, which also eliminates the Na^+ pumped in by the NaCa exchanger in the interval where I_{CaL} is activated [Fig. 2(b)]. The resulting profiles of cytoplasmic concentrations [Fig. 2(c)] are very different from that obtained with $I_S(\mathrm{K}^+)$. Since $[\mathrm{K}_i^+]$ is usually elected as the carrier of intracellular current flow because of its high intracellular concentration [35], we have chosen to restrict the detailed analysis to $I_S(\mathrm{K}^+)$.

2. *Stability*

Figure 3(a) portrays the stability of the fixed points as a function of $I_S(\mathrm{K}^+)$ for the case presented in Fig. 1. The diagram shows the location of the bifurcation points as well as the change in the number of positive real part eigenvalues. The lower branch loses stability through a Hopf bifurcation (Hb1). Close to Hb1, a saddle-node bifurcation (SNb1) leads to the second branch of the diagram. It remains unstable with one real positive eigenvalue until a second Hopf bifurcation (Hb2), which adds a pair of unstable eigenvalues. The upper branch also appears via a saddle-node bifurcation (SNb2), which brings an additional real positive eigenvalue. Hb3, the third Hopf bifurcation, reduces the number of unstable eigenvalues from four to two, and the system finally regains stability through the last Hopf bifurcation Hb4.

Removing the SR (see the earlier presentation of model MnoSR) preserves the z shape of the fixed points but changes the bifurcation structure by eliminating both Hb2 and Hb4 [Fig. 3(b)]. The dynamics of the SR enhances the instability of the system by adding a pair of positive eigenvalues persisting from Hb2 to Hb4. For all fixed points between Hb2 and Hb4, the calcium subsystem (see the earlier presentation of model MonlyCA) is unstable and produces oscillations coming from the lag between the spontaneous calcium release from the SR to the SS and its reuptake from the cytoplasmic compartment. In the complete model, the variations of cytoplasmic and SS $[\mathrm{Ca}^{++}]$ act on the pump, exchanger, and ionic currents to induce (between Hb3 and Hb4) or participate (from Hb2 to Hb3) to the destabilization of the fixed points. Hb2 and the oscillation of the MonlyCA model begin when the SR and SS $[\mathrm{Ca}^{++}]$ are such that the buffering capacities of the two compartments are close to saturation. Perturbations of $[\mathrm{Ca}^{++}]$ and $[\mathrm{Ca}_{ss}^{++}]$ are then amplified by their direct effect on I_{rel}. A similar oscillation of the calcium subsystem has been found in a pacemaker cell model [36], where it is believed to act for initiating and maintaining the heart rhythm [37].

The bifurcation structure of the MnoSR model is identical to that obtained with more simplified versions of the model where all concentrations were frozen to their $I_S = 0$ resting values [models MonlyV1 and MonlyV2; Fig. 3(b)]. Hence, it can be explained by the dynamics of the voltage-gated membrane ionic currents. In the MonlyV2 model, the instability of the middle branch is spawned by the I_{CaL} conductance. The branch has only one unstable eigenvalue. On one hand, removing or adding any set of gate variables from the Jacobian does not change the stability. On the other hand, stability is regained by removing the contribution of I_{CaL} to the membrane conductance.

Still in the MonlyV2 model, the situation is more complex for the unstable section of upper branch where the stability is controlled by gate variables. The activation gate variable of I_{CaL} (d) is dominant. For most fixed points, it is the only gate variable whose removal stabilizes the Jacobian, whereas the Jacobian containing only the variables V and d is unstable. However, in the latter case, the reduced two-dimensional Jacobian has only one positive eigenvalue, whereas there are two for the complete MonlyV2 model. Doing a forward search for the minimum number of gate variables to include to get two positive eigenvalues, we found that two or three gate variables were necessary. In each case, there were multiple doublets or triplets mostly involving, besides d, the slow inactivation gate variables of the I_{CaL} (f) and/or the activation gate variables of I_{Kr} and I_{Ks}. Hence the instability of the upper branch results from interaction between the activation of I_{CaL}, its much slower inactivation, as well as the slow activation of I_{Kr} and/or I_{Ks}.

3. *Cycles*

The upper trace of Fig. 3(a) shows the amplitude of the TNNP stable cycles existing around the top branch of fixed points. The stable cycles appear close to Hb4 through a cycle saddle-node bifurcation. The associated branch of unstable cycles (not shown) connects with Hb4, which is a subcritical Hopf bifurcation. The stable cycles persist a little beyond SNb1, where they disappear through an homoclinic bifurcation by hitting the middle branch of unstable fixed points between I_S(SNb1) and I_S(Hb1). There are two regimes of oscillation: low-amplitude cycles, starting at Hb4 and finishing a little

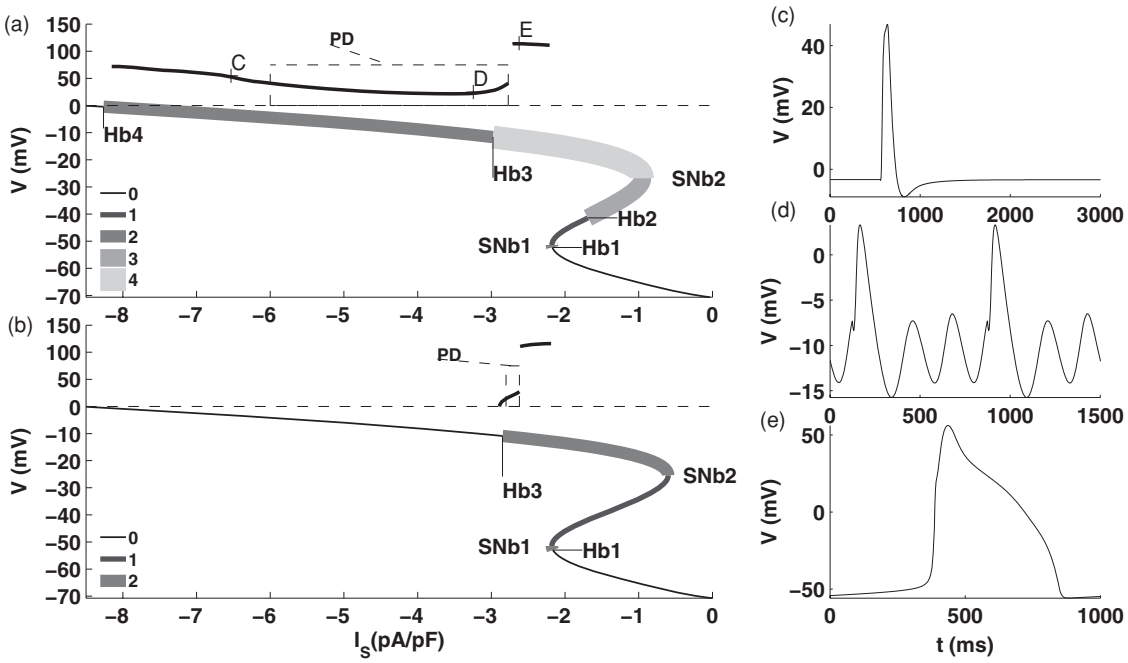

FIG. 3. (a, b) Fixed points and amplitude of the stable cycles as a function of $I_S(K^+)$ ($[K_o^+] = 10mM$, $G_{Katp} = 0$) for the TNNP (a) and MonlyV2 (b) model. The MonlyV2 bifurcation structure is similar to that of the MnoSR model. In each panel, the lower continuous curve gives V of the fixed points. The positions of the Hopf (Hb) and saddle-node (SNb) bifurcations are indicated, as well as the number of unstable eigenvalues shown by the thickness and color of the curve. The upper thick black line gives the amplitude of the stable cycles. Note that the scale of the ordinate is not uniform. The box, labeled PD, indicates the interval where successive period doubling of the cycles is observed. (c–e) Stable cycles of the TNNP model for the I_S values indicated by the corresponding letters in (a).

beyond Hb3 [e.g., Figs. 3(c) and 3(d)], followed by high-amplitude cycles ending at the homoclinic bifurcation [Fig. 3(e)]. There is an abrupt transition between the two oscillatory regimes. Before Hb3, the low-amplitude cycles go through a sequence of period doubling before losing stability. On the other hand, the high-amplitude cycle appears near Hb3 through a cycle saddle-node bifurcation. Although AUTO was not able to completely track the unstable low-amplitude cycles and the branch of unstable high-amplitude cycles created at the cycle saddle-node bifurcation, the result suggests that these two sets of unstable solutions are connected.

As we have discussed, removing the SR stabilizes the system for $I_S < I_S$(Hb3), and the instability of the fixed point between Hb3 and SNb2 then depends on the interaction of the gate variables of I_{CaL}, I_{Kr}, and/or I_{Ks}. The upper trace of Fig. 3(b) shows the evolution of the amplitude of the stable cycles of the reduced MonlyV2 model. Low-amplitude cycles start at Hb3, which has become a supercritical Hopf bifurcation. However, the behavior for increasing I_S is very similar to that of the complete model. The low-amplitude cycles disappear after a sequence of period doubling, to be replaced by high-amplitude cycles that appear through a cycle saddle-node bifurcation and vanish by a homoclinic bifurcation. Hence, even if the SR is responsible for the oscillations occurring between Hb3 and Hb4, the complex cycle bifurcations sequence occurring beyond Hb3 is driven by the membrane Ca^{++} and K^+ currents. To identify the process responsible for the low- and high-amplitude cycles, we studied the effect of G_{Ks} and G_{Kr}, the conductivity of the I_{Kr} and I_{Ks} currents, on the evolution of the cycles in the MonlyV2 model. Decreasing G_{Kr} did not change the nature of the oscillations. However, lowering G_{Ks} by 50% or more led to the disappearance of both the period-doubling sequence and the the abrupt jump from low- to large-amplitude oscillations. The amplitude of the cycle, still created by the supercritical Hb3, was rather slowly growing until vanishing through a homoclinic bifurcation.

In summary, for $[K_o^+] = 10mM$ and $G_{Katp} = 0$, increasing the potassium injury current induces an interesting sequence of stable states: stable-point, large-amplitude cycles, and complex and then simple low-amplitude oscillations.

B. Effect of K_o

As for the Luo-Rudy model [38], the sole augmentation of K_o depolarizes the resting state without altering its stability. However, it can change the bifurcation structure as a function of $I_S(K^+)$.

Comparison of Figs. 4(a), 3(a), and 4(b) ($[K_o^+] = 5.4$, 10, and $18mM$, respectively) shows a depolarization of the fixed points, as well as a reduction of the extent of the middle branch. The evolution of the two saddle-node bifurcations (SNb1, SNb2) fixing the limits of the middle branch can be followed in Fig. 4(c). As $[K_o^+]$ increases, their separation diminishes until they merge at $[K_o^+] = 22mM$. Beyond this value, the $V(I_S)$ curve of the fixed points becomes monotonic decreasing.

A second important transformation is the evolution of the respective positions of Hb1, Hb2, and SNb1. Hb2, the SR-driven Hopf bifurcation, always remains around $V \simeq -41$ mV. As $[K_o^+]$ increases, SNb1, Hb1, and Hb2 come

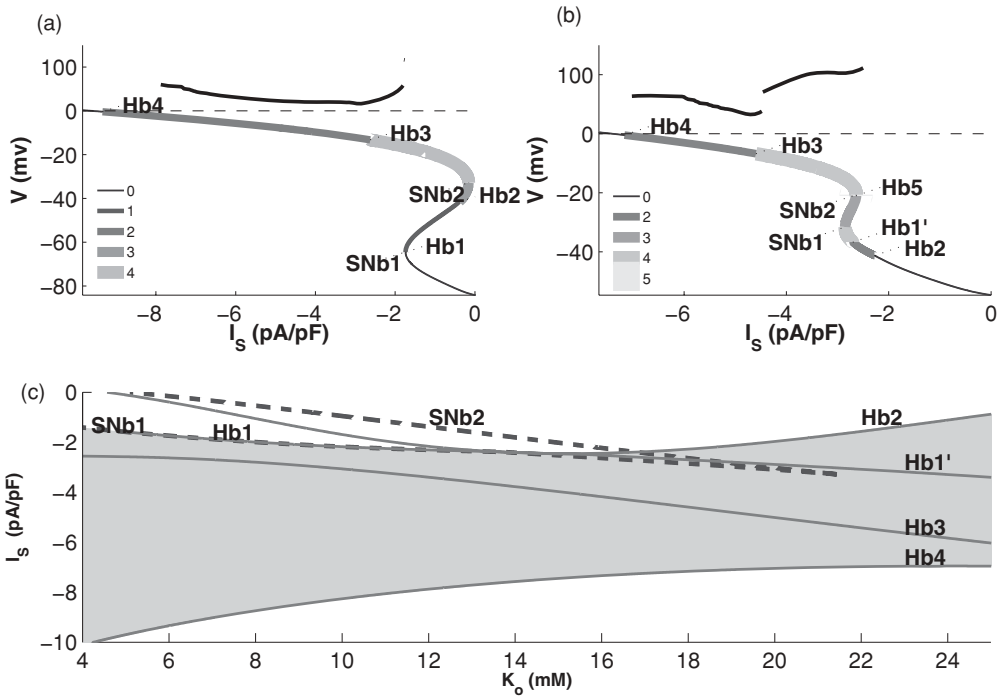

FIG. 4. (a, b) Fixed points and amplitude of the stable cycles as a function of $I_S(K^+)$ for $G_{Katp} = 0$ (a) $[K_o^+] = 5.4mM$, (b) $[K_o^+] = 18mM$. In each panel, the lower continuous curve gives V of the fixed points. The position of the Hopf (Hb) and of the saddle-node (SNb) bifurcations are indicated, as well as the number of unstable eigenvalues, shown by the thickness and color of the curve. The upper thick black line gives the amplitude of the stable cycles. Note that the scale of the ordinate is not uniform. (c) Codimension-2 bifurcation diagram, showing the evolution of the main bifurcations as a function of $I_S(K^+)$ and $[K_o^+]$.

closer to one another until Hb1 disappears at $[K_o^+] = 15mM$. Beyond this value, Hb2 becomes the first bifurcation appearing on the lower branch of fixed points [e.g., Fig. 4(b)]. Below $[K_o^+] = 15mM$, the interval of automaticity extends from Hb4 to ∼Hb1, but from Hb4 to Hb2 for $[K_o^+] > 15mM$ [gray area in Fig. 4(c)]. From $[K_o^+] = 11$ to $22mM$, multiple secondary Hopf bifurcations also exist between SNb1 and Hb1 (until it disappears at $[K_o^+] = 15mM$) or SNb2 and Hb2 [$[K_o^+] > 15mM$, e.g., Fig. 4(b)]. All these bifurcations vanish between $[K_o^+] = 16$ and $22mM$, except for the one labeled HB1′ in Figs. 4(b) and 4(c).

For all values of $[K_o^+]$, stable small-amplitude oscillations exist from Hb4 to Hb3. They lose stability through a sequence of period-doubling bifurcations just beyond Hb3 to be replaced by large-amplitude cycles. These persist until ∼Hb1, for $[K_o^+] < 15mM$, or Hb2, for $[K_o^+] > 15mM$. Below $[K_o^+] = 15mM$, the large-amplitude oscillations disappear through a homoclinic bifurcation, hitting the middle branch of fixed points between $I_S(SNb1)$ and $I_S(Hb1)$. Beyond $[K_o^+] = 15mM$, they rather disappear by hitting the unstable cycles produced by the subcritical Hb2 bifurcation, which means that they are created by a cycle saddle-node bifurcation. This change of scenario is also associated to a transformation of the large-amplitude cycles, which, close to Hb2, display waveform with secondary depolarization similar to EAD (Fig. 5). Increasing $[K_o^+]$ enlarges the width of I_S interval between Hb3 and SNb1 as well as Hb3 and Hb2. As seen in Figs. 4(a), 3(a), and 4(b), this enlargement comes with an increase of the jump in amplitude from stable small to large oscillations and with an extension of the I_S interval over which large oscillations exist.

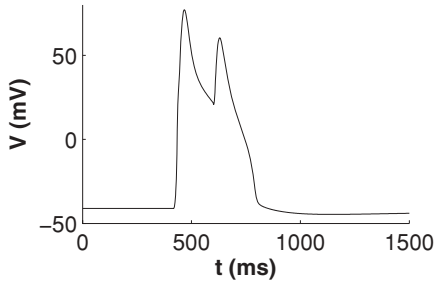

FIG. 5. Action potential displaying early-after-depolarization (EAD)-type reactivation, $[K_o^+] = 18mM$, $I_s = 2.2$ pA/pF, $G_{Katp} = 0$.

C. Effect of I_{Katp}

I_{Katp} is a repolarizing current, removing K^+ ions from the cell. Therefore, its opening should protect against injury current-related ectopic activity. However, unlike I_S, I_{Katp} has a dependency on both V and the potassium Nernst potential, E_k [Eq. (3)].

Figure 6(d) shows the evolution of the main bifurcations as a function of G_{Katp}. Figures 4(a) and 6(a)–6(c) ($G_{Katp} = 0$, 1.2, 1.8, and 2, $[K_o^+] = 5.4mM$) show a slight gradual hyperpolarization of the fixed points. However, increasing G_{Katp} has a similar effect on the middle branch than raising $[K_o^+]$: a higher conductance leads to the disappearance of the branch. Furthermore, both Hb1 and Hb3 disappear such

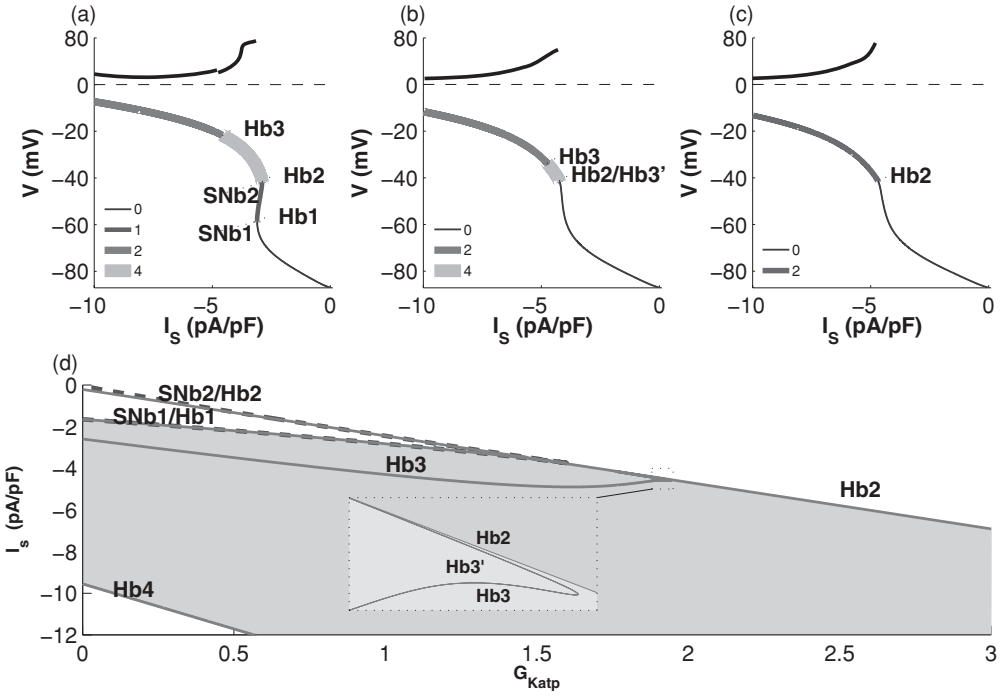

FIG. 6. (a, b, and c) Fixed points and amplitude of the stable cycles as a function of $I_S(\mathrm{K}^+)$ for $[\mathrm{K}_o^+] = 5.4\mathrm{m}M$ and $G_{\mathrm{Katp}} = 1.2$, 1.8, and 2.0. Same representation as that in Figs. 3 and 4(c). (d) Codimension-2 bifurcation diagram, showing the evolution of the main bifurcations as a function of $I_S(\mathrm{K}^+)$ and G_{Katp} for $[\mathrm{K}_o^+] = 5.4\mathrm{m}M$.

that the system finally ends up only with Hb2 and Hb4, which set the limits between the unstable fixed points and the stable oscillations. The disappearance of Hb1 and then Hb3 is preceded by the occurrence of multiple Hopf bifurcations in tiny $[I_S, G_{\mathrm{Katp}}]$ intervals of the parameter spaces.

As long as SNb1 exists ($G_{\mathrm{Katp}} \leqslant 1.6$), the large stable oscillations disappear through a homoclinic bifurcation by hitting the middle branch close to $I_S(SNb1)$. When SNb1 and SNb2 disappear, the oscillation rather ends by connecting with the unstable cycle created at Hb2, which has become a subcritical Hopf bifurcation, as described for high $[\mathrm{K}_o^+]$ in the previous section. We have also observed that the jump from small to large oscillation was always occurring close to Hb3, and that the magnitude of this jump was linked to the extent of the I_S interval between Hb3 and the end of the high-amplitude oscillation. A similar phenomenon is observed with G_{Katp}. Since increasing G_{Katp} initially reduces the distance between Hb3 and the upper limit of automaticity and finally suppresses Hb3, it decreases and then eliminates the discontinuous transition between the two modes of oscillations.

D. Volume of automaticity

Globally, hyperkalemia (Fig. 4) decreases the width of the interval of automaticity, mainly by shifting upward $I_S(Hb4)$, the lower bound of the interval. By decreasing $I_S(Hb3)$, it also enlarges the interval with high-amplitude cycles. On the other hand, increasing G_{Katp} (Fig. 6) enlarges the interval of automaticity, but through a linear decrease of both the I_S upper and lower bounds. The same transition from a homoclinic to a cycle saddle-node bifurcation occurs when the middle branch of fixed points disappears. However, as Hb3 comes closer to the upper bound, the interval with a strictly high-amplitude solution is reduced and disappears with Hb3.

Figure 7 presents the volume of automaticity in the $[I_S, [\mathrm{K}_o^+], \mathrm{K}_{\mathrm{Katp}}]$ three-dimensional (3D) parameter space. The I_S versus $[\mathrm{K}_o^+]$ parabolic upper bound is maintained but is shifted negatively as G_{Katp} increases. The lower bound is also shifted negatively, such that the volume of automaticity enlarges. Since the region is wider at normal $[\mathrm{K}_o^+]$ and closed I_{Katp}, it suggests that the border zone, where $[\mathrm{K}_o^+]$ goes from normal to hyperkalemia and $I_S(\mathrm{K}^+)$ reaches its maximum would be the more susceptible to generate ectopic activity. The thick dashed line surrounds the region of the parameter space where

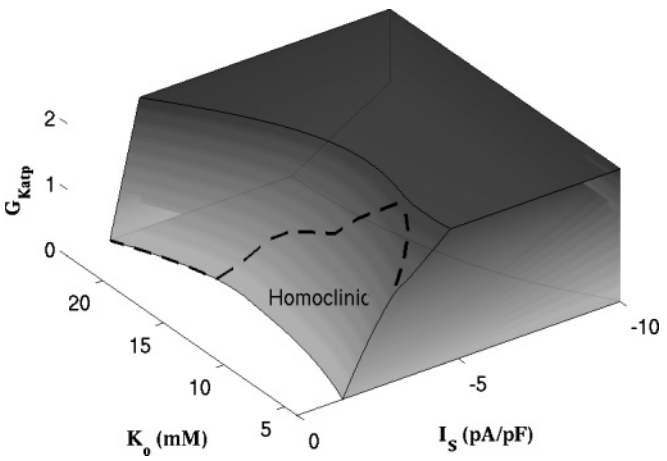

FIG. 7. Volume of automaticity; the thick dashed line encloses the region where the cycle is created by a homoclinic bifurcation. Beyond, it appears through a cycle saddle-node bifurcation.

the cycles appears through a homoclinic bifurcation. It extends over a smaller $[K_o^+]$ interval as G_{Katp} increases.

IV. DISCUSSION

With parameters at their nominal values, (normal $[K_o^+]$ and closed I_{Katp}) the TNNP model exhibits stable automatic activity for $I_S \lesssim -2$ pA/pF. Such current amplitude can be attained in acute ischemia since experimental [39] and modeling [12] studies have suggested that injury current could reach a level beyond -3 pA/pF. As seen in Fig. 7, the increase of $[K_o^+]$, which is known to reach a plateau value of $\sim$15mM [2,10,11] during the first stage of ischemia, does not have an important effect on the upper I_S boundary of the zone of automaticity. Similarly, in Figs. 6 and 7, even a three-fold increase of the I_{Katp} maximum conductivity shifts only the upper bound of the automatic region by ~ -4 pA/pF for all $[K_o^+]$ values. Since the time course of [ATP] is much slower than $[K_o^+]$ and its effect on I_{Katp} is partially counteracted by $[Mg^{++}]$ accumulation, it is unlikely for the increase of I_{Katp} to have much effect on the limits of the zone of automaticity, although it was demonstrated that even a modest increase can induce an important shortening of the action potential duration and an increase of the inward current needed to sustain propagation. [13,14].

The curves giving the voltage of the fixed points as a function of I_S (Figs. 3, 4, and 6) can also be regarded as single-value functions $I_S(V)$, which incidentally were well fitted by third-order polynomials. Considering only $[K_o^+]$, bringing together the curves obtained for the different $[K_o^+]$ provides a two-dimensional function $I_S = f(V,[K_o^+])$. In a one-, two-, or three-dimensional monodomain tissue model, I_S is the current injected by the neighbors, corresponding to $S_v^{-1}\nabla\cdot(D\nabla V)$, in which D is the tensor of intracellular conductivity and S_v the cytoplasmic surface to volume ratio. Hence, it is possible to obtain the stationary voltage distribution associated to any spatial profile of $[K_o^+]$ by solving the system:

$$\frac{1}{S_v}\nabla\cdot(D\nabla V) = f(V,[K_o^+(x)]) \tag{12}$$

with some specified boundary condition on V or its spatial derivative. The profile of $[K_o^+]$ could be fixed empirically or based on models of the extracellular medium such as Refs. [10] or [12].

Alternatively, $[K_o^+]$ can also be expressed as a function of V and I_S to compute the spatial profile of $[K_o^+]$ leading to a given stationary profile of V. However, there is no simple method to assess the stability of nonconstant stationary V profiles in the full reaction-diffusion system including the TNNP model (e.g., for review, Ref. [40]). It is possible to somewhat get around the problem by discretizing the spatial derivatives, obtaining a high-dimensional ODE system that can be linearized around any stationary solution to study its stability.

The results of the single-cell stability analysis offer a fast way to build stationary solutions that can be used either for further analysis or as initial conditions for numerical simulations. Stationary profiles lying partially in the region of isolated cell automaticity would be particularly interesting. Numerous studies have investigated the dynamics of pacemaker cells surrounded by excitable tissue, particularly regarding sinus node models (e.g., Refs. [41–45]). The general conclusion was that coupling conductance, relative pacemaker size, and oscillation amplitude were all critical for propagation. Oscillations have also been observed in models of coupled depolarized and normal cells [38,46] if the flow of axial current was large enough. In all cases, the single-cell bifurcation diagrams may also help to understand the stability of the stationary solutions. Figure 7 shows that any spatial profile crossing the volume of automaticity will enter and exit in a region where the isolated cells start to oscillate through either a homoclinic or a cycle saddle-node bifurcation. This will fix the gradient of autonomous frequency of the oscillators in the medium. The trajectory inside the automaticity volume may either stay in the region with high-amplitude cycles, which always exists close to the boundary, or transit through the area with complex or simple low-amplitude autonomous cycles. These factors, as well as the length of the trajectory inside the automaticity volume, will also impact the capacity of the oscillators to synchronize and drive the entire tissue.

Another interesting aspect is the possibility for transient or bursting-like reactivation [47], caused by current flow during repolarization. A gradient of action potential durations exists at the border between the normal and ischemic tissue, which in repolarization produces currents acting as the injury current. It may then occur that some cells will transiently cross the region of automaticity. Since high-amplitude cycles exist near the border, activation and repolarization could then be seen as moving the system between a stable fixed point and a stable cycle, a typical scenario for early-after-depolarization (EAD) and EAD-like bursting, which could lead to reactivation of the tissue. After-depolarizations induced by the injury current have been previously observed both experimentally [48,49] and in modeling [50].

The present work is far from a comprehensive model of ischemia even at the single-cell level. Ischemia leads to a depletion of the metabolism of the cell, which precedes the interruption of the electron transport chain. This is associated with a shift to anaerobic glycolysis, producing lactic acid. In addition, aerobic respiration normally spends some of the protons that are liberated by the use of ATP. These changes yield to an acidification that alters the conductivity of different ion channels. (For a detailed review of ion channels and cardiac ischemia, see Refs. [2,51]). The TNNP model lacks a representation of the energy metabolism and PH regulation. Chen *et al.* [52] have presented a model including these mechanisms, which was followed by the work of Michailova *et al.* [15]. The latter suggested that the foremost implication for the action potential was from the I_{Katp} channels, which is why their formulation of the current was added to the TNNP model.

The TNNP model is a deterministic lumped compartment model that ignores the stochasticity of both the gate-controlled ionic currents and the calcium-release mechanism. Experimental works have highlighted the localized nature of the ryanodin receptors (RyRs) and CICR (see Refs. [53,54] for review). RyRs are assembled into arrays of calcium release units (CRUs) that display stochastic quantized Ca^{++} release or calcium sparks. Restrepo *et al.* [55] have developed a model of stochastic and spatially distributed CRUs coupled with a deterministic model of rabbit ventricular cells. This model

shows how the nature of CRUs can lead to complex dynamics within the cell [56] and can drive the formation of delay after repolarization [57]. Rovetti *et al.* [58], working on alternative stochastic model of intracellular calcium, have studied how Ca^{++} diffusion allows a CRU's calcium spark to propagate.

The stochasticity of gate-controlled ionic currents has also been studied. In the 1970s, Lecar *et al.* [59,60] showed the implication of the stochastic nature of ion channels for the depolarization threshold. This led to different representations of the neuron stochastic processes (for review, see Refs. [61, 62]). Models of cardiac myocytes have also demonstrated that ion-channel stochasticity might be involved in the generation of after-depolarization and arrhythmia [63–65].

Further work is needed to build a realistic tissue model that includes a representation of the perfusion of the external medium by the blood flow coupled to a mono- or bidomain description of the tissue, or even a more detailed electro-diffusive [66,67] or discrete approach [68]. The incorporation of stochastic localized CRUs within the volume of the cell requires very fine subcellular discretization. The simulation of a 3D ischemic tissue at that spatial scale remains beyond the capability of available computing facilities. Despite these limitations, this paper shows the complexity of single-cell dynamics in a deterministic lumped compartment model and forms a basis for investigating the dynamics of more realistic structures.

ACKNOWLEDGMENTS

This work was supported by funding from the Natural Sciences and Engineering Research Council of Canada, MITACS, and the Québec Heart and Stroke Foundation.

[1] D. Lloyd-Jones *et al.*, Circulation **121**, 568 (2010).
[2] E. Carmeliet, Physiol. Rev. **79**, 917 (1999).
[3] M. Potse, A.-R. LeBlanc, R. Cardinal, and A. Vinet, in: *Proceedings of the 28th Annu. Int. Conf. IEEE EMBS, NY, USA*, pp. 3899–3902 (2006).
[4] A. G. Kléber, Cardiovasc. Res. **45**, 111 (2000).
[5] R. A. Li, M. Leppo, T. Miki, S. Seino, and E. Marbn, Circ. Res. **87**, 837 (2000).
[6] B. Rodríguez, N. Trayanova, and D. Noble, Ann. N. Y. Acad. Sci. **1080**, 395 (2006).
[7] J. P. Keener, J. Cardiovasc. Electrophysiol. **14**, 1225 (2003).
[8] K. H. W. J. ten Tusscher, D. Noble, P. J. Noble, and A. V. Panfilov, Am. J. Physiol. Heart Circ. Physiol. **286**, H1573 (2004).
[9] K. H. W. J. ten Tusscher, and A. V. Panfilov, Am. J. Physiol. Heart Circ. Physiol. **291**, H1088 (2006).
[10] B. Rodriguez, J. M. Ferrero Jr., and B. Trenor, Am. J. Physiol. Heart Circ. Physiol. **283**, H490 (2002).
[11] J. R. Terkildsen, E. J. Crampin, and N. P. Smith, Am. J. Physiol. Heart Circ. Physiol. **293**, H3036 (2007).
[12] M. Potse, R. Coronel, A.-R. LeBlanc, and A. Vinet, in: *Proceedings of the 29th Annu. Int. Conf. IEEE EMBS, Lyon, France*, pp. 6330–6333 (2007).
[13] R. M. Shaw and Y. Rudy, Circ. Res. **80**, 124 (1997).
[14] J. M. Ferrero, J. Saiz, J. M. Ferrero, and N. V. Thakor, Circ. Res. **79**, 208 (1996).
[15] A. Michailova, J. Saucerman, M. E. Belik, and A. D. McCulloch, Biophys. J. **88**, 2234 (2005).
[16] A. Xu and M. R. Guevara, Chaos **8**, 157 (1998).
[17] B. Trénor, L. Romero, J. M. Ferrero, J. Saiz, G. Molt, and J. M. Alonso, Ann. Biomed. Eng. **35**, 1756 (2007).
[18] R. F. Gilmour and D. P. Zipes, Circ. Res. **46**, 814 (1980).
[19] T. Furukawa, S. Kimura, N. Furukawa, A. L. Bassett, and R. J. Myerburg, Circ. Res. **68**, 1693 (1991).
[20] T. R. Shannon, F. Wang, J. Puglisi, C. Weber, and D. M. Bers, Biophys. J. **87**, 3351 (2004).
[21] M. D. Stern, L.-S. Song, H. Cheng, J. S. Sham, H. T. Yang, K. R. Boheler, and E. Ríos, J. Gen. Physiol. **113**, 469 (1999).
[22] A. L. Hodgkin and A. F. Huxley, Am. J. Physiol. **117**, 500 (1952).
[23] J. Kneller, R. J. Ramirez, D. Chartier, M. Courtemanche, and S. Nattel, Am. J. Physiol. Heart Circ. Physiol. **282**, H1437 (2002).
[24] See supplemental material at [http://link.aps.org/supplemental/10.1103/PhysRevE.83.011911] for the complete set of equations and constants of the model.
[25] E. Izhikevitch, *Dynamical System in Neuroscience* (MIT Press, Cambridge, MA, 2007).
[26] J. Guckenheimer and P. Holmes, *Nonlinear Oscillations, Dynamical Systems and Bifurcations of Vector Fields*, Applied Mathematical Sciences Vol. 42 (Springer, New York, 1983) p. 453.
[27] L. Perko, *Differential Equations and Dynamical Systems* (Springer, New York, 1996).
[28] L. Shampine, M. Reichelt, and J. Kierzenka, SIAM Rev. **41**, 538 (1999).
[29] L. Shampine and M. Reichelt, SIAM J. Sci. Comput. **18**, 1 (1997).
[30] B. Krauskopf and H. M. Osinga, in *Numerical Continuation Methods for Dynamical Systems*, edited by J. Galn-Vioque (Springer, New York, 2007).
[31] E. J. Doedel and B. E. Oldeman, [http://indy.cs.concordia.ca/auto/].
[32] A. Vinet and F. A. Roberge, J. Theor. Biol. **147**, 377 (1990).
[33] S. Nagata, S. Doi, and S. Kumagai, MWSCAS '04, the 2004 47th Midwest Symposium on Circuits and Systems, vol. 1 (2004), pp. 393–396.
[34] R. M. Gulrajani, *Bioelectricity and Biomagnetism* (Wiley, New York, 1998).
[35] T. J. Hund, J. P. Kucera, N. F. Otani, and Y. Rudy, Biophys. J. **81**, 3324 (2001).
[36] V. A. Maltsev and E. G. Lakatta, Am. J. Physiol. Heart Circ. Physiol. **296**, H594 (2009).
[37] V. A. Maltsev and E. G. Lakatta, Heart Lung Circ. **16**, 335 (2007).
[38] B. E. Peercy and J. P. Keener, SIAM J. App. Dyn. Sys. **4**, 679 (2005).

[39] M. J. Janse, F. J. van Capelle, H. Morsink, A. G. Kléber, F. Wilms-Schopman, R. Cardinal, C. N. d'Alnoncourt, and D. Durrer, Circ. Res. **47**, 151 (1980).
[40] N. Britton, *Reaction-Diffusion Equations and Their Application to Biology* (Academic Press, London, 1986).
[41] J. K. J. Sneyd, *Mathematical Physiology* (Springer, New York, 2004).
[42] R. L. Winslow, D. Cai, A. Varghese, and Y.-C. Lai, Chaos Solitions Fractals **5**, 491 (1995).
[43] H. Zhang, A. V. Holden, I. Kodama, H. Honjo, M. Lei, T. Varghese, and M. R. Boyett, Am. J. Physiol. Heart Circ. Physiol. **279**, H397 (2000).
[44] A. Tveito and G. T. Lines, Math. Biosci. **213**, 141 (2008).
[45] R. Artebrant, J. Appl. Math. **2009**, 17 (2009).
[46] V. Jacquemet, Phys. Rev. E **74**, 011908 (2006).
[47] A. Shilnikov, R. L. Calabrese, and G. Cymbalyuk, Phys. Rev. E **71**, 056214 (2005).
[48] R. Kumar and R. W. Joyner, Pflugers Arch. **428**, 425 (1994).
[49] A. O. Verkerk, M. W. Veldkamp, N. de Jonge, R. Wilders, and A. C. van Ginneken, Cardiovasc. Res. **47**, 124 (2000).
[50] C. Nordin and Z. Ming, Am. J. Physiol. Heart Circ. Physiol. **268**, H2440 (1995).
[51] W. C. Stanley, F. A. Recchia, and G. D. Lopaschuk, Physiol. Rev. **85**, 1093 (2005).
[52] F. F. Chen, R. D. Vaughan-Jones, K. Clarke, and D. Noble, Prog. Biophys. Mol. Biol. **69**, 515 (1998).
[53] A. Zahradníkov, M. Gaburjáková, J. H. B. Bridge, and I. Zahradník, J. Gen. Physiol. **136**, 581 (2010).
[54] W. Xie, D. X. P. Brochet, S. Wei, X. Wang, and H. Cheng, J. Gen. Physiol. **136**, 129 (2010).
[55] J. G. Restrepo, J. N. Weiss, and A. Karma, Biophys. J. **95**, 3767 (2008).
[56] J. G. Restrepo and A. Karma, Chaos **19**, 037115 (2009).
[57] W. Chen, J. Wasserstrom, and Y. Shiferaw, Am. J. Physiol. Heart Circ. Physiol. **297**, H171 (2009).
[58] R. Rovetti, X. Cui, A. Garfinkel, J. N. Weiss, and Z. Qu, Circ. Res. **106**, 1582 (2010).
[59] H. Lecar and R. Nossal, Biophys. J. **11**, 1048 (1971).
[60] H. Lecar and R. Nossal, Biophys. J. **11**, 1068 (1971).
[61] H. Mino, J. T. Rubinstein, and J. A. White, Ann. Biomed. Eng. **30**, 578 (2002).
[62] I. C. Bruce, Ann. Biomed. Eng. **37**, 824 (2009).
[63] T. Krogh-Madsen, L. Glass, E. J. Doedel, and M. R. Guevara, J. Theor. Biol. **230**, 499 (2004).
[64] C. Lerma, T. Krogh-Madsen, M. Guevara, and L. Glass, J. Stat. Phys. **128**, 347 (2007).
[65] M.-Y. Kim, M. Aguilar, A. Hodge, E. Vigmond, A. Shrier, and L. Glass, Phys. Rev. Lett. **103**, 058101 (2009).
[66] N. Qian and T. Sejnowski, Biol. Cybern. **62**, 1 (1989).
[67] A. Nygren and J. A. Halter, J. Theor. Biol. **199**, 329 (1999).
[68] J. Stinstra, R. MacLeod, and C. Henriquez, Ann. Biomed. Eng. **38**, 1399 (2010).